Available online at www.sciencedirect.com
SCIENCE DIRECT®
Current Applied Physics 4 (2004) 115–120
Current Applied Physics
Physics, Chemistry and Materials Science
www.elsevier.com/locate/cap

Nanoscale pattern formations on surface induced by ion sputtering

Byungnam Kahng [a,*], Jeenu Kim [b]

[a] Center for Theoretical Physics and School of Physics, Seoul National University, Seoul 151-747, South Korea
[b] Supercomputing Research Department, KISTI, Daejeon 305-806, South Korea

Abstract

We investigate diverse pattern formations on sputter-eroded surfaces such as ripples, dots, holes, wires structures. The morphological evolution of ion bombarded surface can be described by the nonlinear Kuramoto–Sivashinsky (KS) equation. Here by performing numerical integration of the KS equation, we show that the diverse pattern formations can be controlled by adjusting experimental conditions such as incidence angle and energy of ion beam.

PACS: 68.55.−a; 05.45.−a; 64.60.Cn; 79.20.Rf
Keywords: Ion sputtering; Kuramoto–Sivashinsky equation; Pattern formation; Nanoscale structures

1. Introduction

The evolution of surface morphology during ion sputtering is a complex phenomenon which induces roughening and smoothing processes. The balance of roughening and smoothing processes leads to pattern formations on surface. Recently many studies have been carried out for such pattern formations on sputter-eroded surface in relation to the fabrication of nanoscale devices.

The fabrication of nanoscale surface structures such as quantum dots and quantum wires have attracted considerable attention due to their applications in optical and electronic devices [1]. These nanostructures form thanks to various self-assembled mechanisms, induced by the combined effect of strain and growth kinetics. Yet, the strained nanostructures obtained by these methods have a size distribution wider than required by applications, and display random alignment. Lithographic methods [2] are often considered prime candidates to overcome these shortcomings, but their limited resolution offers further challenges. Consequently, there is continued high demand for alternative methods that would allow low cost and efficient mass fabrication of nanoscale surface structures. In the light of these technological and scientific driving forces, the recent demonstration by Facsko et al. that low-energy (40 eV–1.8 keV) normal incident Ar^+ sputtering on GaSb (1 0 0) surfaces leads to nanoscale islands which display remarkably good hexagonal ordering and have a uniform size distribution, has captured the interest of the scientific community [3,4].

Experimental studies on ion sputtered surfaces, covering amorphous and crystalline materials (SiO_2 [5]), and both metals (Ag [6]) and semiconductors (Ge [7], Si [8,9]), have motivated extensive theoretical work aiming to uncover the mechanism responsible for such nanoscale pattern formation and kinetic roughening. A particularly successful model has been proposed by Bradley and Harper (BH) [10], in which the height $h(x, y, t)$ of the eroded surface is described by the linear equation

$$\partial_t h = v_x \partial_x^2 h + v_y \partial_y^2 h - K\nabla^4 h, \tag{1}$$

where v_x and v_y are effective surface tensions generated by the erosion process, and K is the surface diffusion constant. The balance of the unstable erosion term $(-|v|\partial^2 h)$ and the smoothing surface diffusion term $(-K\partial^4 h)$ generates ripples with wavelength $\ell_i = 2\pi\sqrt{2K/|v_i|}$, where i refers to the direction (x or y) along which the associated v_i (v_x or v_y) is the largest. When the incidence angle θ is close to grazing (normal), the ripple wave vector is perpendicular (parallel) to the component of the ion beam. While successful in predicting the ripple wavelength and orientation [11], this linear theory cannot explain a

* Corresponding author.
E-mail address: kahng@phya.snu.ac.kr (B. Kahng).

1567-1739/$ - see front matter © 2003 Elsevier B.V. All rights reserved.
doi:10.1016/j.cap.2003.10.010

number of experimental features such as (i) the wavelength of ripple structure being independent of temperature in low temperature regime, (ii) the saturation of the ripple amplitude [12–14], (iii) the observation of rotated ripples [15], and (iv) the appearance of kinetic roughening [16,17]. These phenomena can be explained by the noisy nonlinear equation, called the Kuramoto–Sivashinsky (KS) equation [18],

$$\frac{\partial h}{\partial t} = v_x \frac{\partial^2 h}{\partial x^2} + v_y \frac{\partial^2 h}{\partial y^2} + \frac{\lambda_x}{2}\left(\frac{\partial h}{\partial x}\right)^2 + \frac{\lambda_y}{2}\left(\frac{\partial h}{\partial y}\right)^2 - D_{xy}\frac{\partial^4 h}{\partial x^2 \partial y^2} - D_{xx}\frac{\partial^4 h}{\partial x^4} - D_{yy}\frac{\partial^4 h}{\partial y^4} - K\nabla^4 h + \xi(x,y,t), \tag{2}$$

where λ_x and λ_y describe the tilt-dependent erosion rates in each direction; D_{xx}, D_{yy}, and D_{xy} are the ion induced effective diffusion constants; and $\xi(x,y,t)$ is an uncorrelated white noise with zero mean, mimicking the randomness resulting from the stochastic nature of ion arrival to the surface [18,19]. At low temperatures all the coefficients in Eq. (2) depend on experimental parameters such as the ion beam energy ϵ and the incidence angle of ion beam θ [20], which are given in Appendix A. In low temperature limit, the thermal diffusion term is not relevant, while in high temperature limit, the ion induced diffusion term, i.e., the D-term is not relevant. For the sputter erosion process, $v < 0$ and $D > 0$, while the signs of λ_x and λ_y vary depending on the incident angle of the ion beam.

When the nonlinear terms and the noise are neglected, Eq. (2) reduces to the linear theory Eq. (1), and predicts ripple formation. It is known that the isotropic KS equation ($v_x = v_y < 0$, $D_{xx} = D_{yy} = D_{xy}/2$, and $\lambda_x = \lambda_y$) asymptotically (for large time and length scales) predicts kinetic roughening, with exponents similar to those seen experimentally in ion sputtering [16]. For positive v_x and v_y, Eq. (2) reduces to the anisotropic Kardar–Parisi–Zhang (KPZ) equation [21], whose scaling behavior is controlled by the sign of $\lambda_x \cdot \lambda_y$ [22]. Finally, a recent integration by Rost and Krug [23] of the noiseless version of Eq. (2) provided evidence that when $\lambda_x \cdot \lambda_y < 0$, new ripples, unaccounted for by the linear theory, appear and that their direction is rotated with respect to the ion direction [23]. The nonlinear effects have been largely unexplored experimentally due to lack of theoretical predictions of an experimentally detectable signature that distinguishes them from the linear effects. To make specific predictions on the morphology of ion-sputtered surfaces, we need to gain a full understanding of the nonlinear behavior predicted by Eq. (2). In this paper we numerically integrate Eq. (2), aiming to uncover the dynamics and the morphology of the surfaces for different values of the parameters.

2. Numerical integration

The direct numerical integration is carried out by using standard discretization techniques to discretize the continuum equation, Eq. (2) [24]. Since the sign of the nonlinear terms plays a significant role in defining the surface morphology, we discuss separately the $\lambda_x \cdot \lambda_y > 0$ and $\lambda_x \cdot \lambda_y < 0$ cases.

The $\lambda_x \cdot \lambda_y > 0$ case: A general feature of systems such as Eq. (2) is that the nonlinear terms do not affect the surface morphology or dynamics until a crossover time τ has been reached. Thus, we expect that for early times, i.e., for $t < \tau$, the surface morphology and dynamics are properly described by the linear theory. To demonstrate this separation of the linear and nonlinear regions, in Fig. 1, we show the time dependences of the surface width defined as $W^2(L,t) \equiv \frac{1}{L^2}\sum_{x,y} h^2(x,y,t) - \bar{h}^2$ and of the mean height $\bar{h} = \frac{1}{L^2}\sum_{x,y} h(x,y,t)$. We find that for $t < \tau$, the width W increases exponentially while the mean height stays constant at $\bar{h} = 0$. Furthermore, inspecting the surface morphology, we find that in this region the ripple wavelength and orientation are also correctly described by the linear theory.

While the early time behavior is correctly predicted by the linear theory, beyond the crossover time τ, the nonlinear terms become effective. One of the most striking consequence of these terms is that the surface width stabilizes rather abruptly (see Fig. 1). Furthermore, the ripple pattern generated in the linear region disappears, and the surface exhibits kinetic roughening. The crossover time τ from the linear to the nonlinear behavior can be estimated by comparing the strength of the linear term with that of the nonlinear term [25]:

$$\tau \sim (K/v^2)\ln(v/\lambda), \tag{3}$$

in high temperature limit. In this expression, v, K, and λ refer to the direction perpendicular to the ripple orientation. The predicted λ-dependence of τ is confirmed in the inset of Fig. 1(a). Another quantity that reflects the transition from the linear to the nonlinear region is the

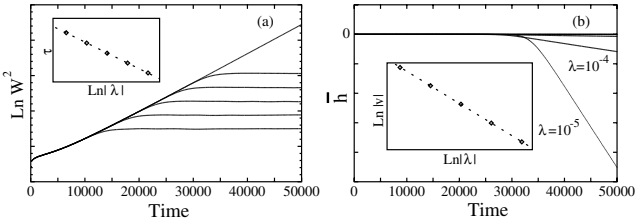

Fig. 1. Time evolution of (a) the surface width W^2 and (b) the mean height $\bar{h}$ for the parameters $v_x = -0.0001$, $v_y = -0.6169$, and $K_x = K_y = K_{xy}/2 = 2$. The different curves correspond to different values of $\lambda_x = \lambda_y = \lambda$. In (a), from top to bottom, the curves correspond to $\lambda = 0$, -10^{-5}, -10^{-4}, -10^{-3}, -10^{-2}, and -10^{-1}, respectively. In (b), from bottom to top, they correspond to $\lambda = -10^{-5}$, -10^{-4}, -10^{-3}, -10^{-2}, and -10^{-1}, respectively. Inset (a): The crossover time τ, estimated from (a) is shown as a function of $\ln|\lambda|$. Inset (b): Plot of $\ln|v|$ versus $\ln|\lambda|$. The dotted line has a slope ≈ -1.07, implying $v \sim 1/\lambda$.

erosion velocity $v = \partial_t \bar{h}$. The nonlinear terms act to decrease the mean height in the case of $\lambda_x < 0$ and $\lambda_y < 0$. We can estimate the surface velocity as $v \sim \lambda W(L,\tau)^2/\ell^2 \sim v^3/(K\lambda)$ using $W(L,\tau) \sim v/\lambda$. This dependence of v on λ is consistent with the numerical results shown in the inset of Fig. 1(b).

The $\lambda_x \cdot \lambda_y < 0$ case: As Fig. 2(a) shows, we again observe a separation of the linear and the nonlinear regions; however, we find that the morphology and the dynamics of the surface in the nonlinear region are quite different from the case $\lambda_x \cdot \lambda_y > 0$. In region I, for early times ($t < \tau$), the surface forms ripples whose wavelength and orientation is correctly described by the linear theory. After the first crossover time τ, given by Eq. (3), the surface width is stabilized, and the ripples disappear. After τ, the system enters a rather long transient region, that we call region II. Here, the surface is rough, and no apparent spatial order is present. We often observe the development of individual ripples, but they soon disappear, and no long-range order is present in the system. However, at a second crossover time, τ_2, a new ripple structure suddenly forms, in which the ripples are stable and rotated with an angle ϕ_c to the x direction. The angle ϕ_c has the value $\phi_c = \tan^{-1}\sqrt{-\lambda_x/\lambda_y}$, (or $\tan^{-1}\sqrt{-\lambda_y/\lambda_x}$) [23].

The demonstrated morphological transitions generate an anomalous behavior in $\bar{h}$ as well. As Fig. 2(a) shows, the mean height is zero in the linear region, increases as the ripples are destroyed in region II, and decreases with a constant velocity in region III. More specifically, ripples are aligned along the y-axis in region I, because $\ell_x \ll \ell_y$. Thus, the contribution of $(\partial_x h)^2$ is much larger than that of $(\partial_y h)^2$, even though $|\lambda_x| < |\lambda_y|$, and the surface height increases due to the term $\lambda_x(\partial_x h)^2$ with $\lambda_x > 0$ in region II. However, as the ripples are destroyed by the nonlinear effects, the contribution of the $(\partial_y h)^2$ term increases, and eventually $\lambda_y(\partial_y h)^2$ becomes larger than $\lambda_x(\partial_x h)^2$, forcing the mean height to decrease because $\lambda_y < 0$. The velocity in region III is determined by the nonlinear coefficient in the direction along the ripples, which reduces to $\lambda_x + \lambda_y$ after a coordinate transformation to the rotated ripple direction. This prediction is in good agreement with the results of Fig. 2(b), which demonstrates that $v \sim 1/(\lambda_x + \lambda_y)$.

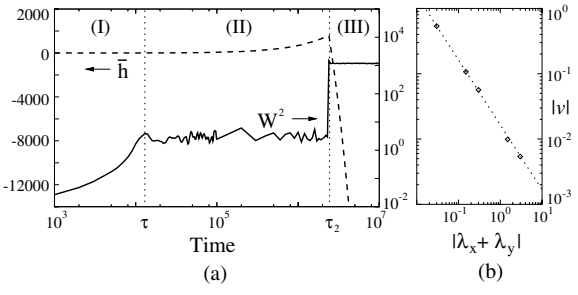

Fig. 2. (a) Time evolution of the mean height $\bar{h}$ (dashed, left linear scale) and the surface width (solid, right logarithmic scale) for the parameters, $v_x = -0.6169$, $v_y = -0.01$, $K_x = K_y = K_{xy}/2 = 2$, $\lambda_x = 1$, and $\lambda_y = -4$. The dotted lines seperate the three regions discussed in the text. (b) The dependence of $|v|$ on the nonlinear terms $|\lambda_x + \lambda_y|$ for the same parameters used in (a). The dotted line has a slope ≈ -1.02, implying $v \sim 1/(\lambda_1 + \lambda_2)$.

3. Nanoscale dot and hole formation

Under normal incidence [26], the coefficients in Eq. (2) are isotropic and are given by [19,20]

$$v \equiv v_x = v_y = -faa_\sigma^2/2a_\mu^2, \tag{4}$$

$$D \equiv D_x = D_y = \frac{D_{xy}}{2} = fa^3a_\sigma^2/8a_\mu^4, \tag{5}$$

$$\lambda \equiv \lambda_x = \lambda_y = \left(f/2a_\mu^2\right)\left(a_\sigma^2 - a_\sigma^4 - a_\mu^2\right), \tag{6}$$

where $a_\mu = a/\mu$ and $a_\sigma = a/\sigma$. The morphology of the ion-sputtered surface at three different stages of time evolution is shown in Fig. 3. Let us first concentrate on the $\lambda > 0$ case (upper panels in Fig. 3). In the early stages of the sputtering process, the surface is dominated by small, wavy perturbations (Fig. 3(a)) generated by the interplay between the ion-induced instability and surface relaxation. However, since the system is isotropic in the (x,y) plane, these ripple precursors are oriented randomly, generating short wormlike morphologies on the surface. After some characteristic time, τ, these structures turn into isolated but closely packed islands, reminiscent of the quantum dots reported experimentally (Fig. 3(b)) [27]. Note that upon a closer inspection one can observe the emergence of hexagonal order in the island positions. As the sputtering proceeds, the supporting surface develops a rough profile, destroying the overall uniformity of the islands (Fig. 3(c)). The magnitudues of the

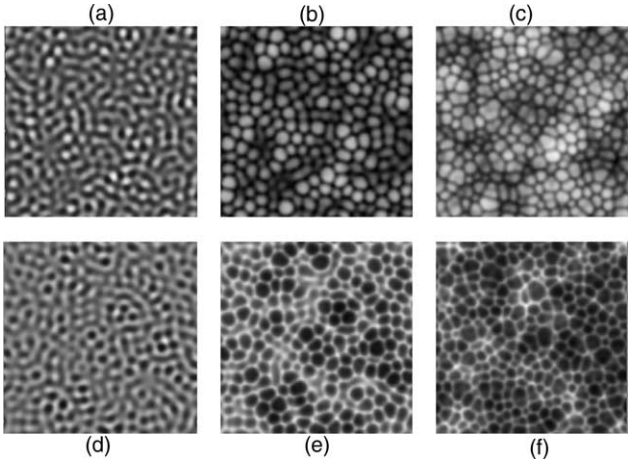

Fig. 3. (a–c) Surface morphologies predicted by Eq. (2) for $\lambda = 1$ at different stages of surface evolution. The pictures correspond to (a) $t = 4.0$, (b) 5.8, and (c) 8.0×10^4. (d–f) are the same as in (a–c), but for $\lambda = -1$. In all cases, we used $v = 0.6169$, $K = 2$, and a system size 256×256.

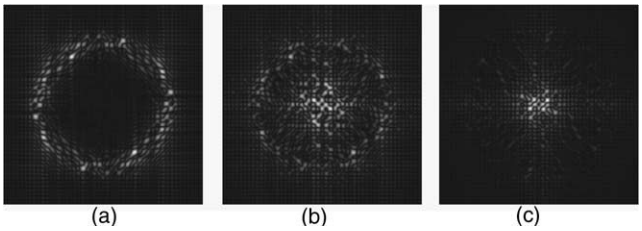

Fig. 4. The amplitudes of the structure factors $|S(\mathbf{q}')|$ for the nanoscale structures in Fig. 3(a–c), respectively.

structure factor for each case of Fig. 3(a)–(c) are given in Fig. 4. A similar scenario is observed for $\lambda < 0$, the only difference being that now the islands are replaced by holes (Fig. 3(d)–(f)). The first conclusion we can draw from these results is that the development of quantum dots and holes is governed by the same underlying physical phenomena, the only difference being that for quantum dots we have $\lambda > 0$, and for holes $\lambda < 0$. Indeed, this morphological change is expected from the nonlinear continuum theory, Eq. (2), being symmetric under the simultaneous transformation $\lambda \to -\lambda$ and $h \to -h$, indicating that changing the sign of λ does not affect the dynamics of the surface evolution, but simply turns the islands into mirrored holes. Since, according to Eq. (5) the sign of λ is determined only by the relative magnitudes of a_σ and a_μ, whether islands or holes appear is determined by the shape of the collision cascade [26]. Consequently, using Eq. (5) we can draw a phase diagram in terms of the reduced penetration depths, a_σ and a_μ, that separate the regions displaying quantum dots and holes [26]. These results also indicate that the quantum dots and holes are inherently nonlinear objects, since, should the linear terms be responsible for their formation, the surface morphology should not depend on the sign of λ (Eq. (1) has a full $h \to -h$ symmetry).

Using Eqs. (3) and (4), we find that $\ell = \sqrt{2}\pi\mu$; i.e., from the average separation of the islands one can determine the size of the horizontal width of the collision cascade [26]. Furthermore, since typically we have $\mu \sim a \sim \epsilon^{2m}$, when ϵ is the ion energy and m is an constant that weakly depend on ϵ ($m = \frac{1}{2}$ for $\epsilon \approx 10$–100 keV), we predict that one can tune the size of the quantum dots by changing the ion energy ϵ, while the size is independent of the flux and the temperature.

4. Nanoscale wire formation

Rotated ripple structures (RRS) form when $\lambda_x\lambda_y < 0$ and the rotation angle is given by $\phi_c = \tan^{-1}\sqrt{-\lambda_x/\lambda_y}$. As shown in Fig. 5, the angle ϕ_c increases with the ratio $a_\mu = a/\mu$, but decreases with the incident angle θ. The KS equation in the rotated frame can be written in the same form as Eq. (2) except that the coefficients v, D, and λ are replaced by v', D', and λ', which are functions

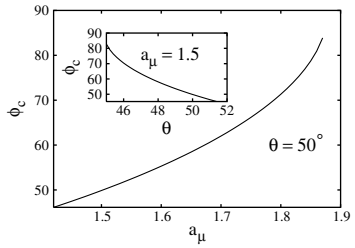

Fig. 5. The rotation angle ϕ_c as a function of a_μ at $\theta = 50°$. The inset shows ϕ_c versus θ for $a_\mu = 1.5$. The rotation angle increases as the ratio a_μ increases, but decreases with the incidence angle θ.

of those in the original frame and the angle ϕ_c. In the rotated frame one of the coefficients of the nonlinear terms, say $\lambda'_{x'}$, is equal to zero, and the other is given by $\lambda'_{y'} = \lambda_x + \lambda_y$, where (x', y') represents the coordinates in the rotated frame. Since $\lambda'_{x'}$ vanishes, the dynamic equation in the x' direction becomes linear. Consequently, the ripple pattern is along the x' direction as long as (i) $v'_{x'} < 0$; (ii) $D'_{x'x'} > 0$; and (iii) $\lambda_x\lambda_y < 0$. Therefore the conditions (i), (ii), and (iii) are the necessary conditions for the formation of the RRS.

We investigate the satisfiability of these conditions in the parameter space $(\theta, a_\mu = a/\mu)$ for different values of $a_\sigma = a/\sigma$. We find that when $a_\mu > 1$ and $a_\sigma = 1$ or $a_\mu > 2$ and $a_\sigma = 2$, the RRS can form in the region depicted in Fig. 6. For $a_\mu < 1$ given $a_\sigma = 1$, the shaded region satisfying (i)–(iii) scarcely exists, so that the formation of RRS is less likely. That means the RRSs are expected to form when the longitudinal width σ is larger than the transverse width μ, that is, $\sigma > \mu$. Recent experimental results indicate that for graphite surfaces σ depends on ϵ, while μ is independent of ϵ for large ϵ (2–50 keV) [28]. Therefore, the $\sigma > \mu$ condition can be met when the energy of the incident ion beam is high enough. Thus in order to obtain the RRS experimentally it is desirable to use high energy ion beam with an appropriate choice of the incidence angle (Fig. 6). However, the use of a high energy ion beam increases τ_2 in Fig. 2 rapidly, requiring a longer exposure time.

Since the nonlinear term disappears in the x' direction the surface in this direction is driven by a linear instability. The amplitude of the RRS grows exponentially with time until the nonlinear term in the y' direction

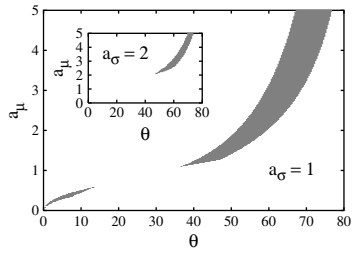

Fig. 6. The shaded region in the parameter space (θ, a_μ) for $a_\sigma = 1$ (inset: for $a_\sigma = 2$) corresponds to the region where the RRS can form.

becomes effective, after which the amplitude saturates. Meanwhile, the surface in the y' direction displays kinetic roughening due to the presence of the nonlinear term $\lambda'_{y'}(\partial_{y'}h)^2/2$, so that the roughness in the y' direction is considerably reduced compared with the roughness in the x' direction. Therefore the RRS develops a rough morphology in the x' direction, while it is relatively smooth in the y' direction, the end configuration resembling a V-shaped wire pattern, as shown in Fig. 7 [29]. The RRS formed in the nonlinear regime is comparable with the ripple pattern formed in the linear regime, where there are modulations in both directions, and the roughness in each direction is almost of the same order.

We also examined the structure factor

$$S(\mathbf{q}) = \int \frac{d\mathbf{r}}{(2\pi)^2} \exp(i\mathbf{q}\cdot\mathbf{r}) H(\mathbf{r}), \tag{7}$$

where $H(\mathbf{r})$ is the height–height correlation function,

$$H(\mathbf{r},t) = \left\langle \sum_{\mathbf{r}'} h(\mathbf{r}'+\mathbf{r},t)h(\mathbf{r}',t) \right\rangle - \left\langle \sum_{\mathbf{r}'} h^2(\mathbf{r}',t) \right\rangle, \tag{8}$$

averaged over different configurations [30]. We find that the structure factor exhibits a peak at $(q_{x,c}, q_{y,c})$, corresponding to $(q'_{x',c}, 0)$ in the rotated coordinates (Fig. 8).

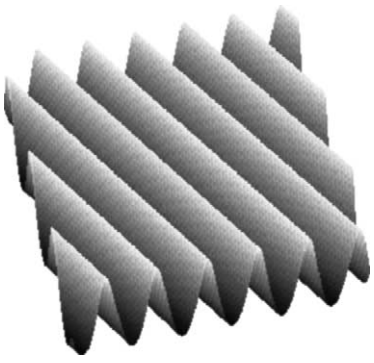

Fig. 7. Surface morphology of the RRS, as generated by numerical simulations, with $a_\mu = 1.3$, $a_\sigma = 1$ and $\theta = 43.56°$.

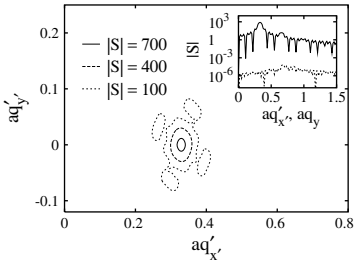

Fig. 8. The amplitude of the structure factor $|S(\mathbf{q}')|$ for the RRS shown in Fig. 7. The peak of the structure factor is at $aq'_{x',c} = 0.33$ and $q'_{y',c} = 0$, implying that the wire structure is straight along the y' axis. The inset shows the comparison between the amplitudes of the structure factor for the RRS (solid line) and for the linear ripple (dotted line), implying the amplitude of the RRS is about a factor of 10^7 larger compared to that of the ripple structure formed in the linear regime.

The fact that $q'_{y',c} = 0$ confirms that the RRS is straight in the y' direction. Moreover, the amplitude of the structure factor for the RRS is much larger compared to the ripple formed in the linear regime, as shown in the inset of Fig. 8. Accordingly, the RRS could be a good candidate for the fabrication of nanowires [31].

5. Conclusion

We have examined diverse pattern formations on sputter-eroded surfaces in terms of the KS equation. Such pattern formations are closely related to experimental observations. We also proposed the possibility of the RRS formation, potential candidates for nanowires for electron transport. We predicted that the RRS can be generated under high energy ion beam, in contrast with the formation of nanoscale dots structure occurring during low energy ion beam sputtering. Since high energy ion beam causes longer crossover time for the formation of the RRS, exposure time of the ion beam has to be adjusted to obtain the desired RRS.

Acknowledgement

This work is supported by the KOSEF Grant No. R01-041-D00061.

Appendix A

$$v_x = a\frac{a_\sigma^2}{2f^3}\left\{2a_\sigma^4 s^4 - a_\sigma^4 a_\mu^2 s^2 c^2 + a_\sigma^2 a_\mu^2 s^2 c^2 - a_\mu^4 c^4\right\}, \tag{A.1}$$

$$v_y = -a\frac{c^2 a_\sigma^2}{2f}, \tag{A.2}$$

$$\lambda_x = \frac{c}{2f^4}\left\{a_\sigma^8 a_\mu^2 s^4(3+2c^2) + 4a_\sigma^6 a_\mu^4 s^2 c^4 - a_\sigma^4 a_\mu^6 c^4(1+2s^2) - f^2(2a_\sigma^4 s^2 - a_\sigma^2 a_\mu^2(1+2s^2)) - a_\sigma^8 a_\mu^4 s^2 c^2 - f^4\right\}, \tag{A.3}$$

$$\lambda_y = \frac{c}{2f^2}\left\{a_\sigma^4 s^2 + a_\sigma^2 a_\mu^2 c^2 - a_\sigma^4 a_\mu^2 c^2 - f^2\right\}, \tag{A.4}$$

$$D_{xx} = \frac{a^3}{24}\frac{1}{f^5}\Big\{-4\left(3a_\sigma^2 s^2 f + a_\sigma^6 s^4\right)f^2 + a_\sigma^2 c^2\left(3f^2 + 6a_\sigma^4 s^2 f + a_\sigma^8 s^4\right)f + a_\sigma^2 c^2\left(3f^2 + 6a_\sigma^4 s^2 f + a_\sigma^8 s^4\right)f + 2(a_\mu^2 - a_\sigma^2)c^2\left(15a_\sigma^2 s^2 f^2 + 10a_\sigma^6 s^4 f + a_\sigma^{10} s^6\right)\Big\}, \tag{A.5}$$

$$D_{yy} = \frac{a^3}{24}\frac{1}{f^5}\frac{3a_\sigma^2}{a_\mu^2}\left\{f^4 c^2\right\}, \tag{A.6}$$

$$D_{xy} = \frac{6a^3}{24}\frac{1}{f^5}\frac{f^2}{a_\mu^2} \times \Big\{ -2(a_\sigma^2 s^2)f^2 + a_\sigma^2 c^2 (f^2 + a_\sigma^4 s^2 f) + 2(a_\mu^2 - a_\sigma^2)c^2(3a_\sigma^2 s^2 f + a_\sigma^6 s^4) \Big\}. \quad \text{(A.7)}$$

In the above expressions, we denoted

$$a_\sigma \equiv a/\sigma, \quad a_\mu \equiv a/\mu, \quad s \equiv \sin\theta, \quad c \equiv \cos\theta, \quad f \equiv a_\sigma^2 s^2 + a_\mu^2 c^2. \quad \text{(A.8)}$$

References

[1] For a review, for example, see L. Jacak, P. Hawrylak, A. Wojs, Quantum Dots, Springer, Berlin, 1998.
[2] T.I. Kamins, R.S. Williams, Appl. Phys. Lett. 71 (1997) 1201.
[3] S. Facsko, T. Dekorsy, C. Koerdt, C. Trappe, H. Kurz, A. Vogt, H.L. Hartnagel, Science 285 (1999) 1551.
[4] F. Frost, A. Schindler, F. Bigl, Phys. Rev. Lett. 85 (2000) 4116.
[5] T.M. Mayer, E. Chason, A.J. Howard, J. Appl. Phys. 76 (1994) 1633.
[6] S. Rusponi, C. Boragno, U. Valbusa, Phys. Rev. Lett. 78 (1997) 2795.
[7] E. Chason, T.M. Mayer, B.K. Kellerman, D.T. McIlroy, A.J. Howard, Phys. Rev. Lett. 72 (1994) 3040.
[8] G. Carter, V. Vishnyakov, Phys. Rev. B 54 (1996) 17647; Z.X. Jiang, P.F.A. Alkemade, Appl. Phys. Lett. 73 (1998) 315.
[9] J. Erlebacher, M.J. Aziz, E. Chason, M.B. Sinclair, J.A. Floro, Phys. Rev. Lett. 82 (1999) 2330.
[10] R.M. Bradley, J.M.E. Harper, J. Vac. Sci. Technol. A 6 (1988) 2390.
[11] I. Koponen, M. Hautala, O-P. Sievaenen, Phys. Rev. Lett. 78 (1997) 2612.
[12] K. Wittmaack, J. Vac. Sci. Technol. A 8 (1990) 2246.
[13] J. Erlebacher, M.J. Aziz, E. Chason, M.B. Sinclair, J.A. Floro, J. Vac. Sci. Technol. A 18 (2000) 115.
[14] J.J. Vajo, R.E. Doty, E-H. Cirlin, J. Vac. Sci. Technol. A 6 (1988) 76.
[15] S. Rusponi, G. Costantini, C. Boragno, U. Valbusa, Phys. Rev. Lett. 81 (1998) 2735.
[16] E.A. Eklund, R. Bruinsma, J. Ruidnick, R.S. Williams, Phys. Rev. Lett. 67 (1991) 1759.
[17] H-N. Yang, G-C. Wang, T-M. Lu, Phys. Rev. B 50 (1994) 7635.
[18] R. Cuerno, A-L. Barabási, Phys. Rev. Lett. 74 (1995) 4746.
[19] M.A. Makeev, A-L. Barabási, Appl. Phys. Lett. 71 (1997) 2800.
[20] M. Makeev, R. Cuerno, A.-L. Barabási, preprint.
[21] M. Kardar, G. Parisi, Y-C. Zhang, Phys. Rev. Lett. 56 (1986) 889.
[22] D.E. Wolf, Phys. Rev. Lett. 67 (1991) 1783.
[23] M. Rost, J. Krug, Phys. Rev. Lett. 75 (1995) 3894.
[24] W.H. Press, B.P. Flannery, S.A. Teukolsky, W.T. Vetterling, Numerical Recipes, Cambridge University Press, Cambridge, 1986.
[25] S. Park, B. Kahng, H. Jeong, A-L. Barabási, Phys. Rev. Lett. 83 (1999) 3486.
[26] B. Kahng, H. Jeong, A-L. Barabási, Appl. Phys. Lett. 78 (2001) 805.
[27] S. Facsko, T. Dekorsy, C. Koerdt, C. Trappe, H. Kurz, A. Vogt, H.L. Hartnagel, Science 285 (1999) 1551.
[28] S. Habenicht, W. Bolse, H. Feldermann, U. Geyer, H. Hofsass, K.P. Lieb, F. Roccaforte, Europhys. Lett. 50 (2000) 209.
[29] E. Kapon, D. Hwang, R. Bhat, Phys. Rev. Lett. 63 (1989) 430.
[30] S.K. Sinha, E.B. Sirota, S. Garoff, H.B. Stanley, Phys. Rev. B 38 (1988) 2297.
[31] J. Kim, B. Kahng, A-L. Barabási, Appl. Phys. Lett. 81 (2002) 3654.